Quantifying microburst wind and turbulence enhancement in canyons

Nicholas T. Luchetti[1], Katja Friedrich[2], Branko Kosović[3]

1 National Weather Service, Raleigh, North Carolina
2 Department of Atmospheric and Oceanic Sciences, University of Colorado, Boulder, Colorado,
3 National Center for Atmospheric Research, Boulder, Colorado

Corresponding Author: Katja Friedrich, Dept. of Atmospheric and Oceanic Sciences, University of Colorado, 4001 Discovery Drive, 311 UCB, Boulder, CO 80309-0311, Email: Katja.Friedrich@colorado.edu

ABSTRACT

Thunderstorms in arid and semi-arid regions like the U.S. intermountain west are often associated with dry microbursts. These microbursts are caused by evaporating precipitation in dry environments causing strong and difficult-to-observe cold outflow boundaries associated with rapid changes in wind and turbulence. A particularly dangerous situation can occur when microburst outflow winds are terrain-channeled into and within canyons during ongoing wildfire events, creating complex tactical challenges for firefighters and emergency managers. Given the dangers to firefighters by unpredictable microbursts and outflow boundaries within canyons, this paper quantifies the canyon-enhancement of wind and turbulence from microburst outflow boundaries using idealized large eddy simulations from the Weather Research and Forecasting (WRF) model. A series of simulations were conducted with the center of microburst downdrafts were placed 1.3 and 3.3 km upwind of a series of canyon types differing in length and slope angle. These canyon simulations are compared to microburst outflow boundary characteristics in flat terrain deriving topographic multiplier and differences in horizontal winds (*wsp*), upward vertical velocity (*w*), and turbulence kinetic energy (*TKE*). The increase in these variables is larger when the microburst is closer to the canyon and for steeper canyon walls generating increase in *wsp* by 4.5-6.6 m s^{-1}, *w* by 1.9-8.4 m s^{-1}, *TKE* by 1.4-6.6 m^2 s^{-2}. The topographic multiplier for horizontal winds is 0.1-0.2 times higher within the long-distance canyons compared to the short-distance canyons.

SIGNIFICANCE STATEMENT

The purpose of this study is understanding how canyons enhance and modify winds associated with thunderstorm microbursts and outflow-boundaries. This is important because changes in wind add complexity and tactical challenges faced by emergency management teams during wildfire events in complex terrain. This study quantifies the changes in wind speed, turbulence, and vertical velocity providing guidance on where the larges changes can be expected depending on the steepness of the canyon and the location of the microburst.

1. Introduction

Thunderstorms are often associated with dangerous downdrafts also referred to as microbursts. Dry microbursts, mainly found in arid and semi-arid regions like the United States intermountain west, develop by evaporation, melting, and sublimation of precipitation causing strong and turbulent ground-level winds that propagate as outflow boundaries radially away from the microburst (Fujita and Wakimoto 1983; Wilson et al. 1984; Fujita 1985). Dry microbursts are often short-lived (< 10 min) with typical diameters of < 4 km and occur with very little rain reaching the surface. As such, they are almost impossible to detect with operational observing networks (Haines 1988; Wakimoto et al. 1994), particularly in mountainous terrain where observational density is sparse and measurements are obscured by the mountains. Microbursts and outflow boundaries in mountain terrain pose a major threat to firefighters' safety as microbursts and outflow boundaries can spread the fire rapidly towards locations that were previously considered safe. Furthermore, terrain itself can enhance and modify microburst and outflow-boundary winds adding complexity and tactical challenges faced by emergency management teams during wildfire events (Goens and Andrews 1998; Sharples et al. 2017). Given the potential threat and the lack of observations, this study quantifies changes in wind speed and turbulence from microbursts and outflow boundaries interacting with canyons and ridges through idealized simulations using the community numerical Weather Research and Forecasting (WRF) model.

Outflow boundaries associated with intense dry microbursts are difficult to predict and observe, given that they are typically associated with high cloud bases and precipitation that evaporates before reaching the ground (Monastersky 1987; Haines 1988; Wakimoto et al. 1994; Potter and Hernandez 2017). Observations of dry microbursts across the intermountain west reveal that many of these events are associated with low radar reflectivity signatures compared to those less complex terrain (Wakimoto et al. 1994), making them difficult to observe by radar (Haines 1988). A deadly example of a dry microburst interaction with a wildfire occurred on 26 June 1990, as hundreds of firefighters fought the Arizona Dude Fire in the hills of the Tonto National Forest northeast of Phoenix, AZ. Surface winds, associated with several dry microbursts developing in the vicinity of the fire, caused the fire to spread in all directions. On the southern side of the fire, these surface winds were enhanced by the local terrain and channeled into a canyon, where six firefighters were killed (Goens and Andrews 1998). Strong surface microburst gusts in combination with complex terrain and wildfires have caused fatalities in other wildfires such as the 1949 Mann Gulch Fire (Rothermel 1993), the 1976 Battlement Fire (USDI 1976), the 1994 South Canyon Fire (USDI/USDA 1994), the 2012 Waldo Canyon Fire (Johnson et al. 2014), the 2013 Arizona Yarnell Hill Fire (Karels and Dudley 2013; Hardy and Comfort 2015; Paez et al. 2015), and the 2015 California Frog Fire (Draeger 2016). Considering the potential safety hazards associated with outflow boundary-induced fire spread in mountainous areas and the lack of observations, the use of high-resolution numerical weather models to accurately simulate thunderstorm outflow boundaries in complex terrain is a research priority for the fire weather community.

Most numerical studies of microburst outflow interactions with terrain have focused on bell-shaped 2-D hills or mountains, and escarpment-like features (Letchford and Illidge 1999; Wood et al. 2001; Mason et al. 2007, 2010). While wildfires can surely be influenced by these types of terrain features (e.g., Hawley 1926; Sullivan 2009; Sullivan et al. 2014), a dangerous situation can also develop when wildfires are terrain-channeled into and within canyons (Goens and Andrews 1998; Brown 2002; Esperanza Investigation Team 2006; Coen and Riggan 2010; Sharples et al. 2010). For example, during the 2006 Esperanza Fire in California, Santa Ana winds aligned with channeled creek drainage flow in a nearby canyon, producing enhanced surface winds and fire behavior which led to the loss of five firefighters (Esperanza Investigation Team 2006; Coen and Riggan 2010). A key finding from the investigation report (Esperanza Investigation Team 2006) was that none of the fire shelters for the deceased firefighters were deployed, suggesting that the head fire must have accelerated as it came through the canyon and caught the firefighters off guard. Another canyon-induced fatality event occurred during the 2001 Thirtymile Fire in Washington where fire-induced winds were channeled up the canyon sidewall killing four firefighters who deployed at a site located 30 m upslope from the valley floor (Brown 2002). An analysis of tree needle heatset observations made at the incident site indicates that fire-induced winds were in the up-canyon and upslope direction, suggesting that the fire's convective column was channeled up the canyon, rather than rising vertically from the surface (Brown 2002). Further analysis suggests that the increased fire spread rate which caught the firefighters off guard likely resulted from a combination of up-canyon winds and downward mixing of stronger upper-level winds which were oriented along the canyon's axis. Explosive fire blow-up and acceleration such as in the events outlined above (1990 Dude Fire; 2001 Thirtymile Fire; 2006 Esperanza Fire) are not rare, especially for wildfires that occur within canyons (Viegas 2005; Viegas and Simeoni 2010). Thus, the combination of hard-to-predict surging microbursts, along with terrain channeling, presents an especially challenging situation for firefighters and emergency managers when responding to wildfires in canyons.

Given the dangers to firefighters by these difficult-to-predict and difficult-to-observe microbursts and outflow boundaries in areas of complex terrain, along with a lack of focus on microburst interactions with canyons in the literature, the aim of this paper is to quantify the canyon-enhancement of wind and turbulence from microburst outflow boundaries. Results are presented describing the influence of short- (1.5 - 4.5 km) and long- (3 - 6 km) distance canyons for a range of upwind and downwind slopes. The influence of microburst location (with respect to the topography) is also discussed. This study is organized as follows: Section 2 discusses the atmospheric model configuration and experimental design. Microburst simulation results and comparisons are presented and discussed in Section 3. Conclusions and suggestions for future work are discussed in Section 4.

2. Methods

a. WRF-LES Configuration

Simulations presented in this study are configured in WRF large-eddy simulation (LES) mode (WRF v3.6), where the most energetically significant turbulent eddies are explicitly resolved (Moeng et al. 2007; Mirocha et al. 2010). This fine-scale (grid spacings of $\Delta \sim 10 - 100$ m) representation of boundary layer turbulence is necessary to resolve the energy-containing turbulent motions that are responsible for most of the turbulent transport. The model is run with one outer 27 km x 27 km domain (d01) and one inner 13.5 km x 13.5 km domain (d02) (Table 1). The d01 has a horizontal resolution of 90 m and uniform terrain-following (eta) coordinates. In the vertical, 73 levels are used with the finest resolution of 10 m in the lowest ⅔ of the domain. The d02 has a horizontal resolution of 30 m, uniform terrain-following (eta) coordinates, and the same 73 vertical levels as the d01. A weakly stable background atmosphere is used with an initial potential temperature of 295 K that increases at 0.005 K m^{-1} up to a planetary boundary layer (PBL) height of z_{pbl} = 750 m, and at 0.001 K m^{-1} through the remainder of the domain up to a z_{top} = 2 km. The Brunt-Vaisala frequency also highlights this weakly stable profile with a frequency of ~0.02 s^{-1} up to the top of the PBL (z_{pbl} = 750 m), followed by a gradual decrease in frequency to 0.01 s^{-1} through the remainder of the vertical profile. To maintain numerical stability and eliminate gravity waves that reflect off the upper boundary, a Rayleigh damper with a damping coefficient of 0.003 s^{-1} is applied near the top of the domains. A constant surface heat flux of 50 W m^2 is applied to both domains to spin up and maintain a realistic turbulent boundary layer throughout the duration of the simulations. The Thompson microphysical scheme is used to represent microphysical processes. For simplicity, short grass is used and applied homogeneously across the domains to represent the land-surface type with a surface roughness length of 0.03 m. Radiative transfer processes are not considered in either domain.

Domain name	**D*x*, *y***	**D*t***	***Nz***	**Dimensions [*x*, *y*, *z*]**
d01	90 m	0.25 s	73	27 km x 27 km x 2 km
d02	30 m	0.13 s	73	13.5 km x 13.5 km x 2 km

Table 1. Domain configurations for the outer (d01) and inner (d02) domain with horizontal resolution (Dx, y), time step (Dt), number of vertical model levels (Nz), and domain dimensions in the x, y, and z directions.

To simulate realistic turbulent inflow into the d02, unaffected by terrain features, one-way nesting is used. Both domains resolve turbulence explicitly using a 1.5 order Turbulence Kinetic Energy (*TKE*), Deardorff closure model, but the d01 uses a “flat-plate” lower surface boundary and periodic conditions (Mirocha et al. 2013; Nunalee et al. 2014). The d01 provides turbulent inflow boundary conditions for the d02, which includes terrain features in the lower surface boundary. To eliminate terrain-induced wake effects being recycled into the inflow turbulence from the d01, feedback between the d02 and the d01 is turned off. This technique allows for the d02 to be fed realistic turbulent inflow without terrain-induced wake features. See Mirocha et al. (2013) and Nunalee et al. (2014) for more details on this technique.

Simulations are run for a total of seven hours, with the first six hours used to “spin up” realistic turbulence across the domains. After turbulence is spun up, analysis is done over the final hour of the simulations (from 6 to 7 h). The six-hour spin-up time is determined by assessing the temporal evolution of horizontally averaged *TKE* near the surface (Fig. 1a). As the d01's flow travels downstream within the d02, the streamwise *TKE* field eventually reaches a developed state characterized by low turbulent fluctuations (Fig. 1b). At z = 250 m, this developed state occurs at x = ~10 km (Fig. 1b). At z = 750 m, the developed state occurs further downstream at x = ~12 km (Fig. 1b). Domain-averaged vertical profiles of potential temperature and the Brunt-Vaisala frequency during hour 6-7 highlight a fully developed weakly stable atmosphere (Fig. 2a -b). Modest low-level shear within the boundary layer, (Fig. 2c), coupled with subtle heat flux forcing produces a weakly stable vertical *TKE* profile characterized by modest turbulence near the surface that rapidly drops off with height up to the top of the PBL (Fig. 2d).

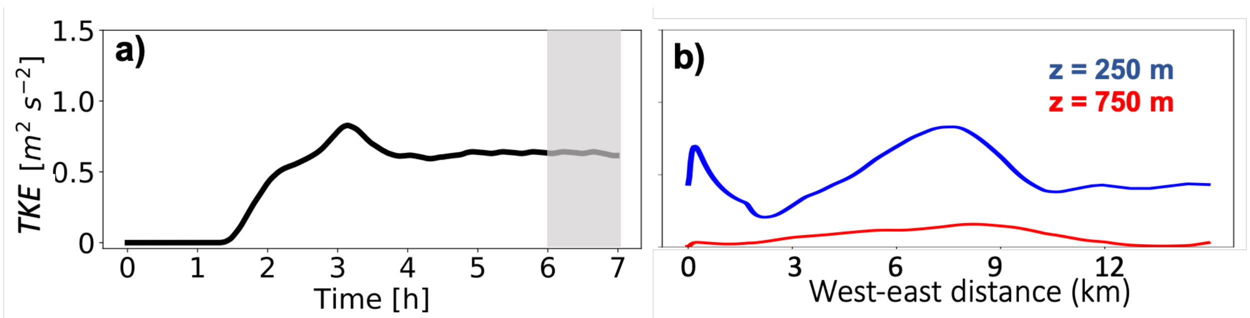

Fig. 1. a) Temporal evolution of *TKE* at 250 m averaged across d02. Gray shading represents the analysis times (6-7 h) presented here. b) West-east cross section of TKE at 250 m and 750 m averaged over the analysis time (6-7 h) in south-north direction.

At t = 6 h, a cold bubble perturbation is introduced into the potential temperature field of the d02 to initiate a downdraft (Grant and Heever 2016; Marion and Trapp 2018). The maximum cold air perturbation of -15 K, also used by Grant and Heever (2016) and Marion and Trapp (2018), is centered at z = 15 m; horizontal center points of the perturbation vary depending on the simulation and will be discussed in section 2b. The perturbation stretches 1 km in the horizontal and 1.5 km in the vertical. In this post-spin-up stable environment, the cold air perturbation descends, reaches the surface, and then produces a cold outflow boundary that propagates radially away from the center of the downdraft. The cold air perturbation of -15 K produces a downburst that is short lived (< 10 min), covers a small spatial area (downdraft diameter < 4 km), and produces strong outflow winds (> 10 m s^{-1}), which is consistent with microburst definitions from previous observational studies (Fujita and Wakimoto 1983; Wilson et al. 1984; Fujita 1985).

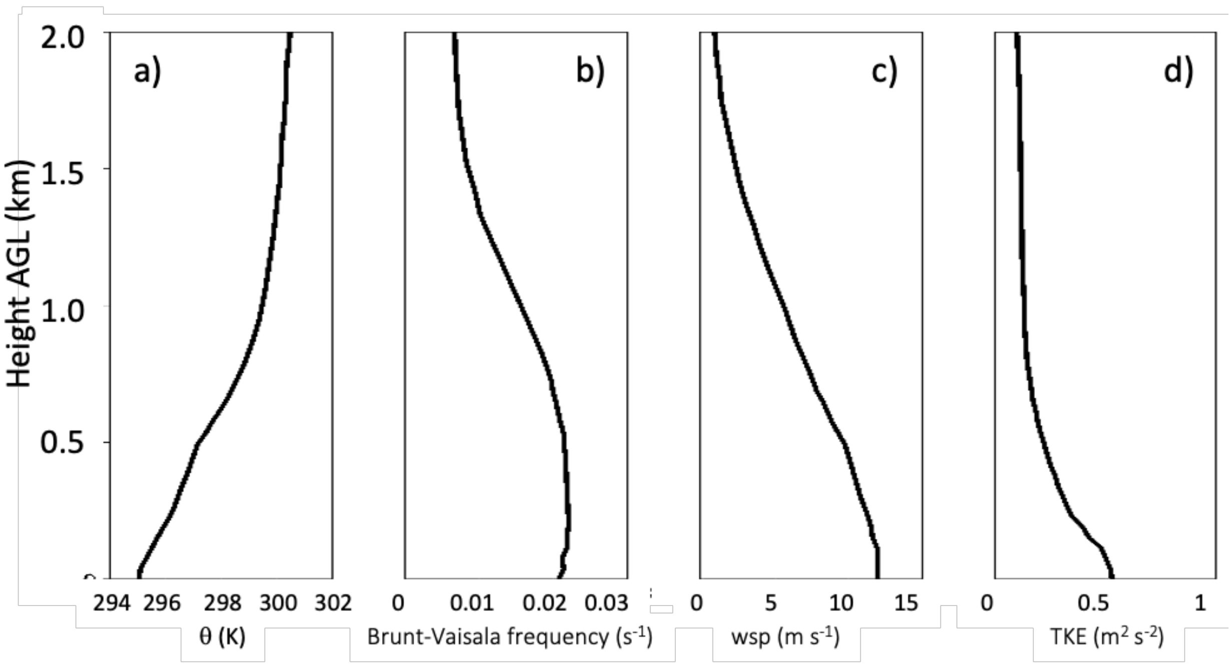

Fig. 2. Vertical profiles of a) potential temperature (θ in K), b) Brunt-Vaisala Frequency (s^{-1}), c) horizontal wind speed (*wsp* in m s^{-1}), and d) resolved turbulent kinetic energy (*TKE* in m^2 s^{-2}) averaged over d02 and 6-7 h.

b. Experimental Design

Microburst outflow boundaries generated by the WRF-LES simulations described above propagate horizontally and interact with canyons placed downwind of where the downdraft impinges onto the surface. To investigate and contrast changes in wind and turbulence by differing canyon types, simulations are run for both short- (~1.5 to 4.5 km) and long-distance canyons (~3 to 6 km) (Table 2). For the short-distance canyons (SC) scenario, two sets of simulations are conducted each with two north-south oriented mountains creating a west-east oriented canyon between them (Fig. 3). In the first set of simulations (referred to as 10°SC; Table 2), the two mountains, each 6 km long and 3 km wide with 10° slopes, create a 2-km wide and 4-km long canyon (Fig. 3a, c). In the second set of simulations (referred to as 30°SC; Table 2), the two mountains, each 3 km long and 1.5 km wide with 30° slopes, create a canyon 1.5-km long and 0.5-km wide (Fig. 3b, d). Both slope scenarios feature a maximum crest height of 250 m, and a length of ~1.5 km across each flat portion of the ridgeline. The horizontal width of the entire ridgeline in the *x*-direction is ~4.8 km for 10°SC and ~1.2 km for 30°SC. The distance from the canyon floor to the top of the ridgeline is ~2.5 km for 10°SC (Fig. 3a, c), and ~0.8 km for 30°SC (Fig. 3b, d). The chosen terrain slopes of 10° and 30° are consistent with typical values used in previous experimental studies on the effects of terrain slope on fire spread rate (Sharples 2008; Dupuy et al. 2011; Liu et al. 2014).

Simulation name	**Canyon Slope**	**Microburst Location**
SHORT-DISTANCE CANYONS (SC)		
SDM10°SC	10°	Short-distance microburst (SDM)
SDM30°SC	30°	Short-distance microburst (SDM)
LDM10°SC	10°	Long-distance microburst (LDM)
LDM30°SC	30°	Long-distance microburst (LDM)
LONG-DISTANCE CANYONS (LC)		
SDM10°LC	10°	Short-distance microburst (SDM)
SDM30°LC	30°	Short-distance microburst (SDM)
LDM10°LC	10°	Long-distance microburst (LDM)
LDM30°LC	30°	Long-distance microburst (LDM)
NO TERRAIN – BASELINE (BL)		
LDM0°BL	0°	Long-distance microburst (LDM)
SDM0°BL	0°	Short-distance microburst (SDM)

Table 2. List of idealized WRF-LES simulations: A set of eight canyon simulations were conducted with 1.5-4.5 km (short-distance canyon; SC) or 3-6 km (long-distance canyon; LC) canyons with 10° and 30° canyon slope and microburst downburst centered either at 1.3 km (short-distance microburst; SDM) or 3.3 km (long-distance microburst; LDM) from the canyon entrance. In addition, two simulations were conducted without terrain for SDM and LDM.

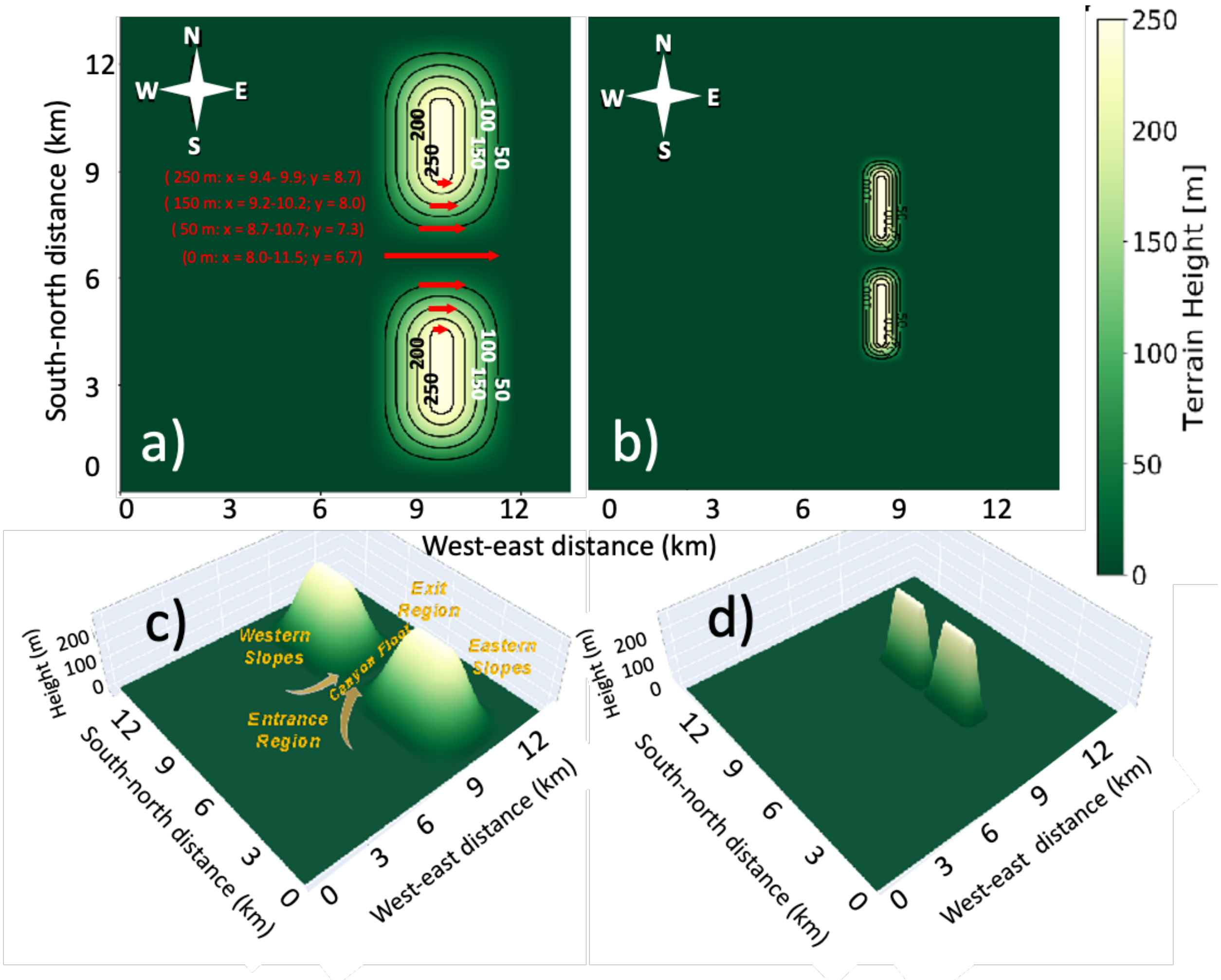

Fig. 3. a-b) Planar and c-d) three-dimensional views of the terrain height for short-distance canyon (SC) simulations with 10° (a, c) and 30° (b, d) mountain slopes. a) For the analysis shown in Tables 3-4 we derive maximum differences in *wsp*, w_{up}, and *TKE* between the baseline and canyon simulations over all time steps along the red arrows the 0, 50, 150, and 250-m contour lines. Red numbers indicate (*x*,*y*) coordinates over which maximum differences are calculated.

For the long-distance canyon (LC) scenario, we use the same mountains as in the SC simulations but rotate them by 90° so that the long-side is now oriented in the east-west direction (Fig. 4; Table 2). By rotating the mountains, the canyon is now 6.5 km long and 3 km wide for the mountains with the 10° slope (referred to as 10°LC; Fig. 4a, c) and 3 km long and 1.5 km wide for the mountains with a 30° slope (referred to as 30°LC; Fig. 4b, d). In each canyon simulation, we refer to the entrance region as the location where the outflow boundary first enters the canyon on the west side, and the exit region where the boundary leaves the canyon on the east side (Fig. 3c).

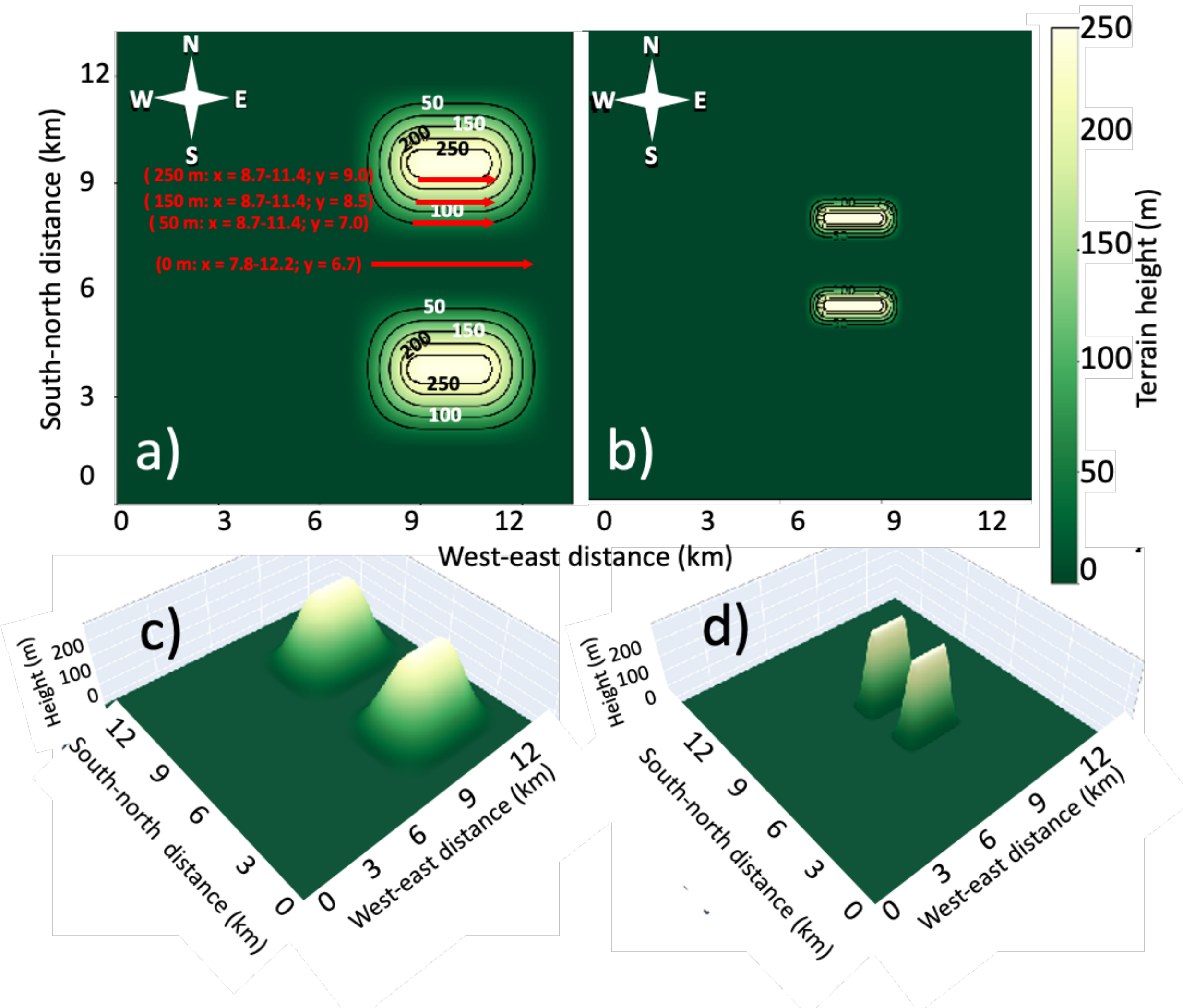

Fig. 4. As Fig. 3, but for the long-distance canyon (LC) simulations.

To study the interactions between microburst wind speed and canyon types, the four canyon simulations (10°SC, 30°SC, 10°LC, 30°LC) are run with a microbursts placed i) near or west of the canyon entrance so that the maximum magnitude in near-surface horizontal outflow boundary winds (wsp_{max}) occurs at the canyon entrances (also referred to as short-distance microburst or SDM simulations; Table 2) and ii) farther west and away from the canyon entrance (or long-distance microburst or LDM simulations). To determine wsp_{max}, a baseline

(BL) simulation of an isolated microburst over flat terrain (Table 2) is run with the microburst placed at x = 6.7 km and y = 6.7 km in the center of the d02 (Fig. 5). wsp_{max} occurs 1.3 km from the center of the downdraft. Thus, the canyon entrance is placed 1.3 km east from the center of the microburst or at x = 8 km for the short-distance microburst (SDM) simulations including the four canyon types (SDM10°SC, SDM30°SC, SDM10°LC, SDM30°LC). To simulate the influence of weaker downburst winds, the center of the microburst is now moved farther upwind from x = 6.7 km to x = 4.7 km for the long-distance microburst (LDM) simulations including four canyon types (LDM10°SC, LDM30°SC, LDM10°LC, LDM30°LC). In the LDM simulations, the canyon entrance remains at x = 8 km, but the center of the microburst is moved from x = 6.7 km to x = 4.7 km, resulting in a 3.3 km distance between microburst center and canyon entrance. To summarize, a total of eight canyon simulations and two baseline simulations (SDM0°BL; LDM0°BL) were conducted (Table 2).

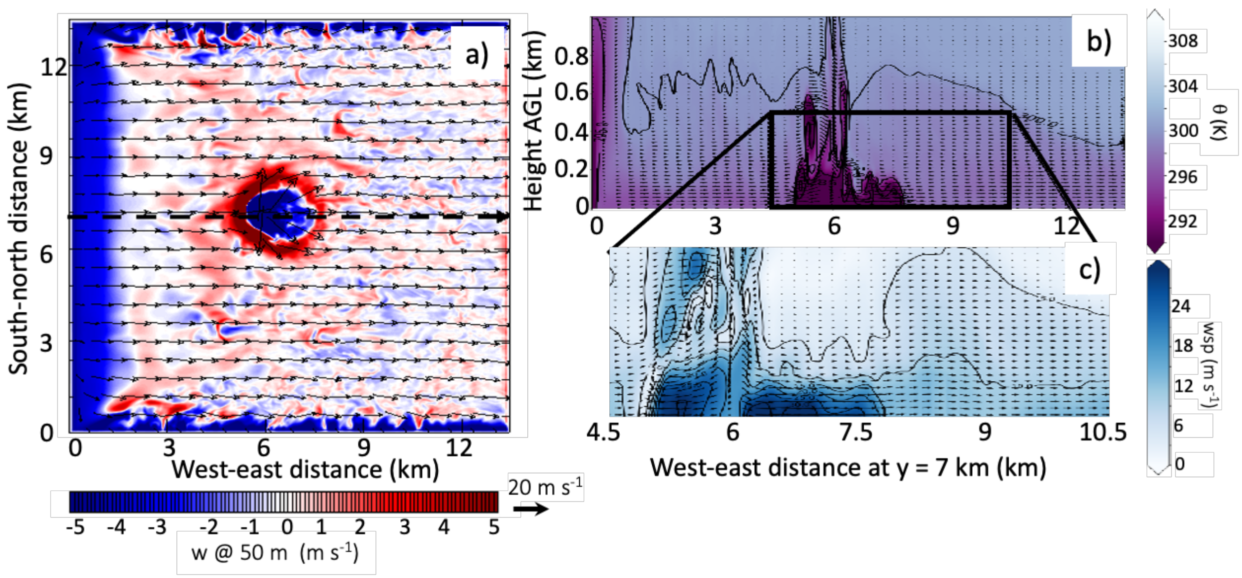

Fig. 5. Baseline simulation microburst structure at the time of maximum horizontal winds at 06h:01min:30s. a) Vertical velocity (m s^{-1}; color-coded) at 50 m AGL (filled colors) and horizontal wind (m s^{-1}; arrows) at the surface. A west-east cross section at y = 6.7 km (black dashed arrow in a) is shown in b-c) with potential temperature θ (K; color-coded) in b) and magnitude of horizontal wind speed (m s^{-1}; color-coded and contours) in c). Vectors show winds in the x-z plane in b-c).

To visualize the role of the terrain on wind speed changes, we generated horizontal maps showing the spatial differences in horizontal wind speed (wsp) at 10 m AGL, vertical velocity

(w) at 50 m, and turbulent kinetic energy (*TKE)* at 10 m between the baseline and the various canyon simulations. Additionally, we calculate the maximum differences in *wsp*, upward w (w_{up}), and *TKE* between the baseline and canyon simulations between 6-7 h at the canyon floor (0 m) and canyon walls across the 50, 150, and 250 m contour isolines in the west-east direction (red arrows in Fig. 3a; numbers indicate (x,y) coordinates over which maximum differences are calculated).

In addition to the west-east horizontal cross-sections, we calculate a topographic multiplier (M_t) to quantify wind enhancement due to topography (Mason et al. 2007, 2010). M_t is the ratio of the horizontal wind speed at a specific height, z, above the canyon, to the wind speed at the same location in the baseline simulation, i.e., simulation without topography. The purpose of M_t is to quantify the increase or decrease in the horizontal wind speed for flow over canyons, by normalizing it against the horizontal wind speed for flow in the 0°BL simulations. For all eight canyon simulations, we calculate the maximum M_t across the west-east cross-sections at 0, 50, 150, and 250 m contours across all time steps using:

$$M_t(z) = \frac{wsp(z)_{canyon}}{wsp(z)_{0°BL}} \quad (1)$$

where $wsp(z)_{canyon}$ is the horizontal wind speed at a height, z, above the canyon and $wsp(z)_{0°BL}$ is the horizontal wind speed at the same location above a flat surface (0°BL). Since microburst outflow winds are generally strongest near the surface, here we calculate M_t values at the lowest model level at z = 10 m AGL.

3. Results

a. Baseline Simulation for Short Distance Microburst

The baseline simulation entails an isolated microburst and associated outflow boundary over flat terrain placed in the center of the d02 (Fig. 5). After the cold bubble perturbation is introduced, the resulting downdraft has a diameter of ~1 km and a maximum downdraft speed of -31 m s^{-1}, consistent with observations of microbursts in dry regions which are typically < 4 km in diameter and feature downdrafts speeds as high as 30 m s^{-1} (Fujita and Wakimoto 1983; Wilson et al. 1984; Fujita 1985). When the descending column of cold air reaches the surface, the flow diverges horizontally away from where the downdraft impinges on the surface (Fig. 5).

The westward moving part of the outflow boundary encounters an ambient 15 m s^{-1} headwind from the west which induces a ring-like vortex feature that extends vertically to ~750 m AGL (Fig. 5b). The ambient headwind decelerates the westward movement of the outflow boundary, confining it close to the downdraft throughout the duration of the simulation. In contrast, the eastward moving horizontal outflow boundary encounters a tailwind, which helps to accelerate it away from the downdraft. However, the eastward moving outflow boundary does not feature a ring-like vortex along the leading edge, likely due to less convergence with the ambient wind field. This is reflected in w depicted in Fig. 5a, where w_{up} is weaker (~1 m s^{-1}) along the leading edge of the eastward moving outflow boundary, compared to the westward moving outflow boundary where convergence with the westerly ambient wind field enhances w_{up} along the boundary to > 5 m s^{-1}. Note that the circular outward fanning of outflow boundary winds from the center of the microburst shown in Fig. 5a is typical of microbursts observed in flat terrain regions (Fujita 1985). Horizontal winds accelerate to a maximum of wsp_{max} = 37 m s^{-1} at z = 10 m within the eastward moving outflow boundary (Fig. 5c). Moving from the center of the downdraft towards the east, wsp_{max} occurs at ~1.3 km from the downdraft at x = 8 km, beyond which, the horizontal wind velocities behind the boundary drop-off rapidly as the cold air outflow entrains warmer ambient air ahead of the boundary.

b. *Short Canyon Simulations*

1) SHORT-DISTANCE MICROBURST

According to density current theory, the larger the temperature difference between the cold air of the density current and the warmer environmental air, the stronger the difference in wind speeds across the different air masses (Benjamin 1968; Simpson and Britter 1980; Jorgensen et al. 2003). Since outflow boundaries often behave like density currents (Charba 1974; Sasaki and Baxter 1986; Friedrich et al. 2005), horizontal winds across the leading edge of the boundary are typically strongest when the boundary is closer to the cold downdraft. In this section, we investigate short-distance microburst wind and turbulence in short canyons with slopes of 10° and 30° (SDM10°SC and SDM30°SC).

The outflow boundary in SDM30°SC propagates faster through the canyon and over the mountains and shows stronger increases in *wsp*, w_{up}, and *TKE* compared to SDM10°SC (Fig. 6). Three minutes after the microburst is initialized in SDM10°SC, the leading edge of the outflow boundary begins to propagate through the canyon and ride up the west-facing slopes and the north- and south-facing canyon walls (Fig. 6a, c, e). In contrast, at this same time step, the outflow boundary in SDM30°SC has already exited the canyon and reached the crest of both mountains (Fig. 6b, d, f). Compared to SDM0°BL, *wsp* is stronger at the exit region on the east side of the canyon (by ~6 m s^{-1}) and atop the crest of the northern mountain (by ~7 m s^{-1}) in SDM30°SC (Fig. 6b). Along the southern mountain's west-facing slope, however, the increase in *wsp* is weaker (by ~2-3 m s^{-1}) compared to the SDM0°BL. In the SDM10°SC, only slightly stronger *wsp* (~2 m s^{-1}) are observed compared to SDM0°BL (Fig. 6a). w_{up} is stronger along the west-facing slopes and the north- and south-facing canyon walls in both SDM10°SC and SDM30°SC compared to SDM0°BL. However, the increase in w_{up} is considerably higher in SDM30°SC (~8 m s^{-1}) compared to SDM10°SC (~2 to 3 m s^{-1}) (Fig. 6c-d). Note that the stronger w_{up} is confined to the west-facing slopes and canyon walls with little to no enhancement within and along the canyon floors of both simulations. Similarly, *TKE* is stronger along the SDM30°SC walls, crest, and eastern slope of the northern mountain (~6 to 7 m^2 s^{-2}) compared to the *TKE* observed along the SDM10°SC canyon walls and west-facing slopes (~0.5 to 1 m^2 s^{-2}). Furthermore, little to no increase in *TKE* is observed along the canyon floors in either SDM10°SC and SDM30°SC simulations compared to SDM0°BL (Fig. 6e-f).

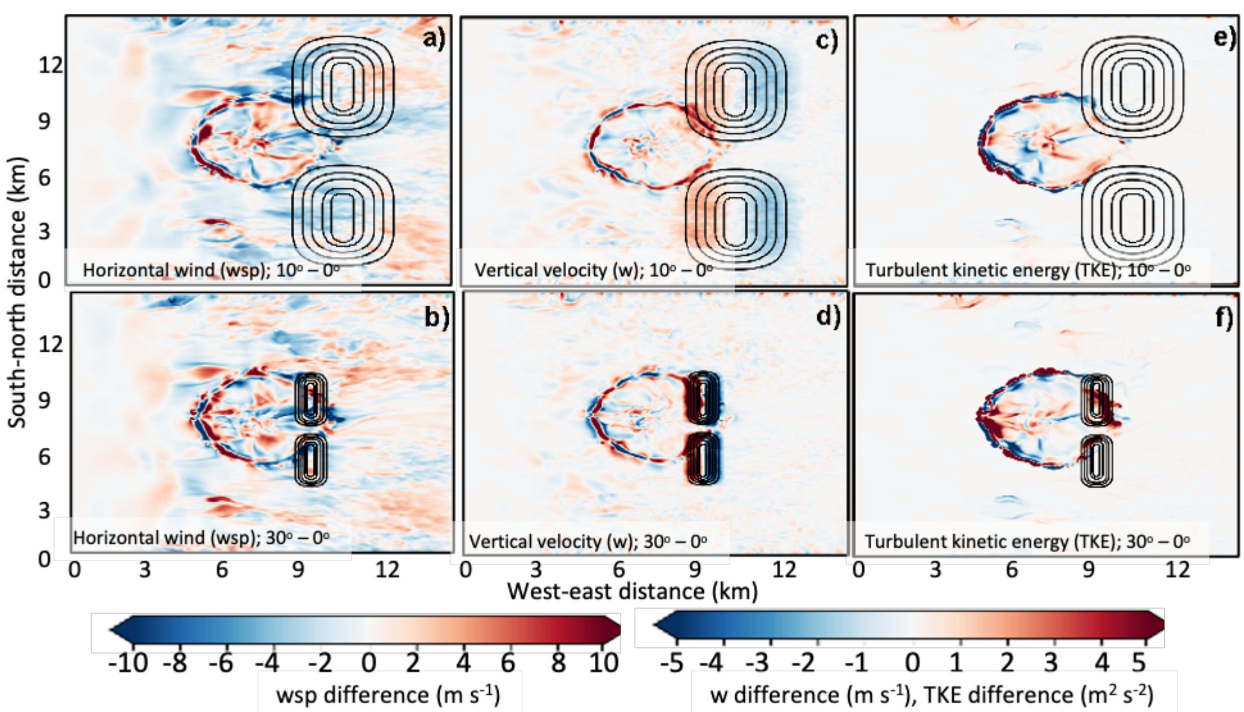

Fig. 6. Differences between a, c, e) SDM10°SC-SDM0°BL and b, d, f) SDM30°SC-SDM0°BL for a-b) wind speed at 10 m (*wsp*; m s^{-1}), c-d) vertical velocity at 50 m (*w*; m s^{-1}), and e-f) turbulent kinetic energy at 10 m (*TKE*; m^2 s^{-2}) at 06h:03min:00s. Terrain is indicated by black lines with 50 m terrain contours.

Five minutes after downdraft initiation (06h:05min:00s), the outflow boundary in SDM10°SC reaches the crest of both mountains and the leading edge has passed through the canyon floor (Fig. 7a, c, e). In contrast, the outflow boundary in SDM30°SC has passed the canyon and mountains (Fig. 7b, d, e). As such, *wsp*, *w*, and *TKE* along the leading edge of the outflow boundary are no longer influenced by the terrain. However, strong upward and downward *w* is still observed along the western and eastern slopes in SDM30°SC (Fig. 7d), highlighting the impact of slopes on *w* for even after the outflow boundary passed. In SDM10°SC, *wsp* at the canyon floor's exit region and along the north- and south-facing canyon walls are up to ~5 m s^{-1} higher compared to SDM0°BL (Fig. 7a). Little to no increase in w_{up} (< 0.5 m s^{-1}) is observed along the SDM10°SC canyon floor (Fig. 7c). However, along the west-facing slopes, canyon walls, and crests of both the northern and southern mountains, w_{up} increases by up to ~4 m s^{-1} along the outflow boundary. Similarly, stronger *TKE* is observed up to ~5 m^2 s^{-2} along both north- and south-facing SDM10°SC walls and west-facing slopes, with little to no increase observed along the canyon's floor.

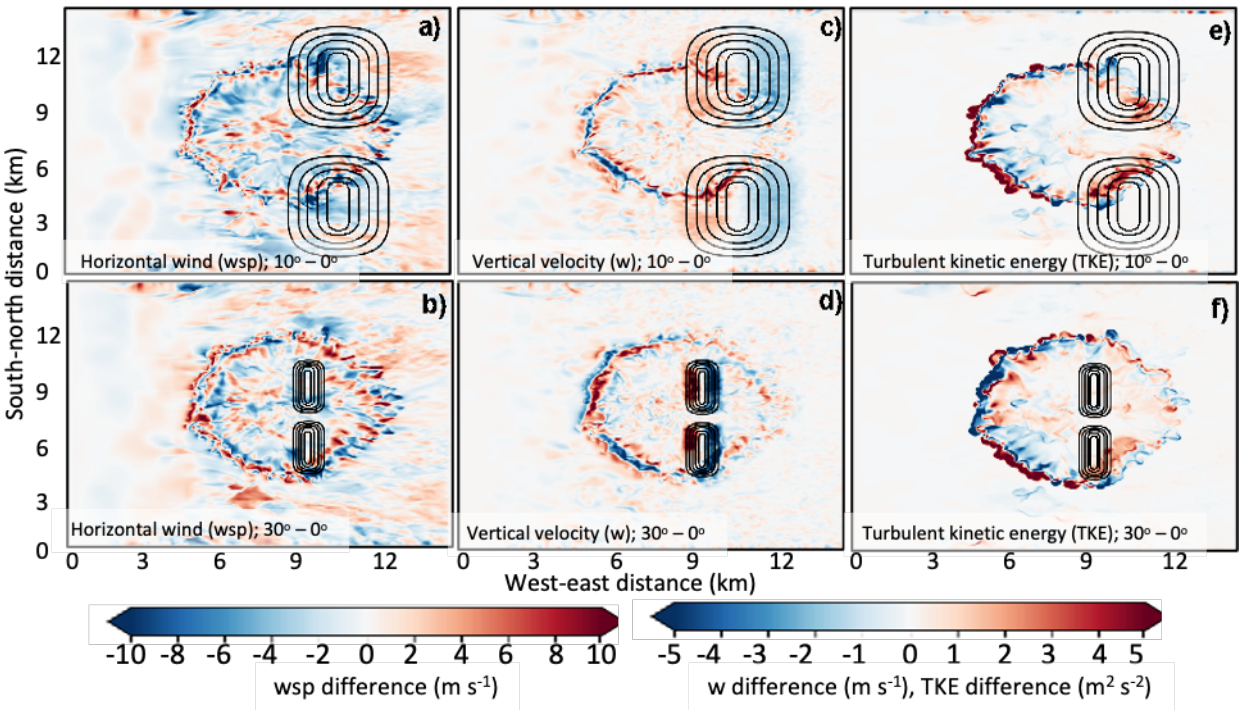

Fig. 7. As Fig. 6, but at 06h:05min:00s.

2) LONG-DISTANCE MICROBURST

As outflow boundaries displace farther from their source of cold air, the winds along the boundary typically diminish according to density current theory. In this section, we investigate wind and turbulence at ridges and canyons when the microburst occurs 3.3 km from the terrain (LDM10°SC, LDM30°SC). Here, the center of the microburst downdraft is moved to 3.3 km from that canyon entrance at x = 4.7 km. Contrary to the SDM simulations, the outflow boundary in LDM30°SC propagates only slightly faster through the canyon and over the mountains and with similar magnitude increases in *wsp* compared to LDM10°SC. About four minutes after downdraft initiation, the outflow boundary reaches the west-facing slopes of the LDM10°SC and propagates almost halfway through the canyon (Fig. 8a, c, e). At the same time, the outflow boundary in LDM30°SC reaches the crest of both mountains and has almost passed through the canyon (Fig. 8b, d, f). Weak increases in *wsp* are observed along the LDM10°SC (~3 to 4 m s^{-1}) and LDM30°SC canyon floors (~3 to 4 m s^{-1}) compared to LDM0°BL (Fig. 8a-b). Additionally, *wsp* increase (~3-4 m s^{-1}) atop the crest and east-facing slopes of the northern LDM30°SC mountain. However, the increase in *wsp* is slightly weaker (~2-3 m s^{-1}) along the west-facing slopes of the southern mountain. In LDM10°SC, little increase in *wsp* is observed along the canyon walls and west-facing slopes (< 2 m s^{-1}) compared to LDM0°BL. Stronger w_{up} is observed along the west-facing slopes and canyon walls in both LDM10°SC (1~2 m s^{-1}) and LDM30°SC (~5 m s^{-1}) compared to LDM0°BL, but with little to no enhancement (< 0.5 m s^{-1}) along either canyons' floor (Fig. 8c-d). Similarly, *TKE* is solely enhanced atop the western slope and crest of the LDM30°SC northern mountain (~4 m^2 s^{-2}), yet negligible enhancement (< 0.5 m^2 s^{-2}) is observed along the canyon walls, floor, and southern mountain (Fig. 8f). For LDM10°SC, *TKE* negligibly increases (~0.5 to 1 m^2 s^{-2}) near the lower north-facing wall of the southern mountain, with little enhancement elsewhere (< 0.5 m^2 s^{-2}) (Fig. 8e).

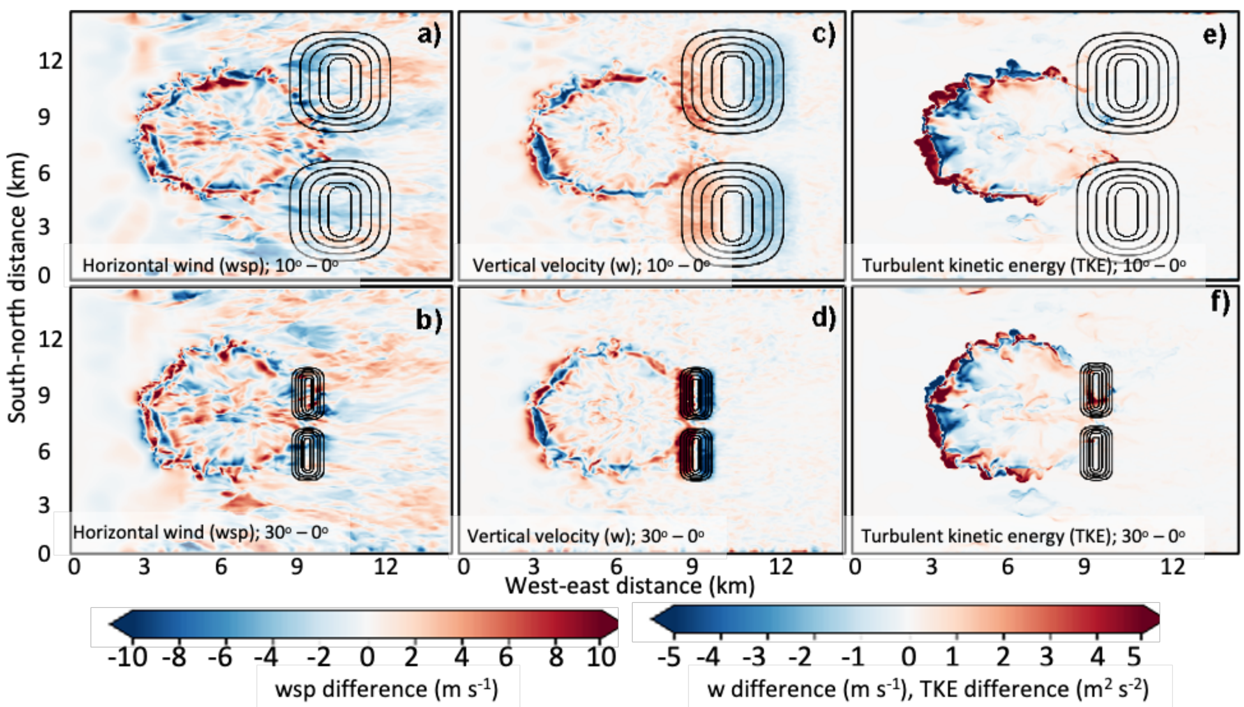

Fig. 8. As Fig. 6, but for differences between a, c, e) LDM10°SC-LDM0°BL and b, d, f) LDM30°SC-LDM0°BL at 06h:04min:03s.

A few minutes later (06hh:06min:30s), the outflow boundary has reached the crests of both mountains and the canyon exit region in LDM10°SC (Fig. 9a, c, e). In contrast, the LDM30°SC outflow boundary has passed the mountains and canyon at this time step (Fig. 9b, d, e). Similar to the short-distance microburst simulation, strong w_{up} (> 5 m s^{-1}) is still observed along both western and eastern slopes in LDM30°SC after the outflow boundary passed the terrain. At the exit region and along portions of the canyon walls, *wsp* is slightly stronger (by ~3 to 4 m s^{-1}) in LDM10°SC compared to LDM0°BL (Fig. 9a). Similarly, w_{up} is stronger by ~2 to 3 m s^{-1} along the west-facing slopes and walls of both the northern and southern LDM10°SC mountains, but less so along the canyon floor (<1 m s^{-1}) (Fig. 9c compared to LDM0°BL). Lastly, the increase in *TKE* between the LDM0°BL and LDM10°SC simulations is ~0.5 to 1 m^2 s^{-2} within and along the floor and walls (Fig. 9e).

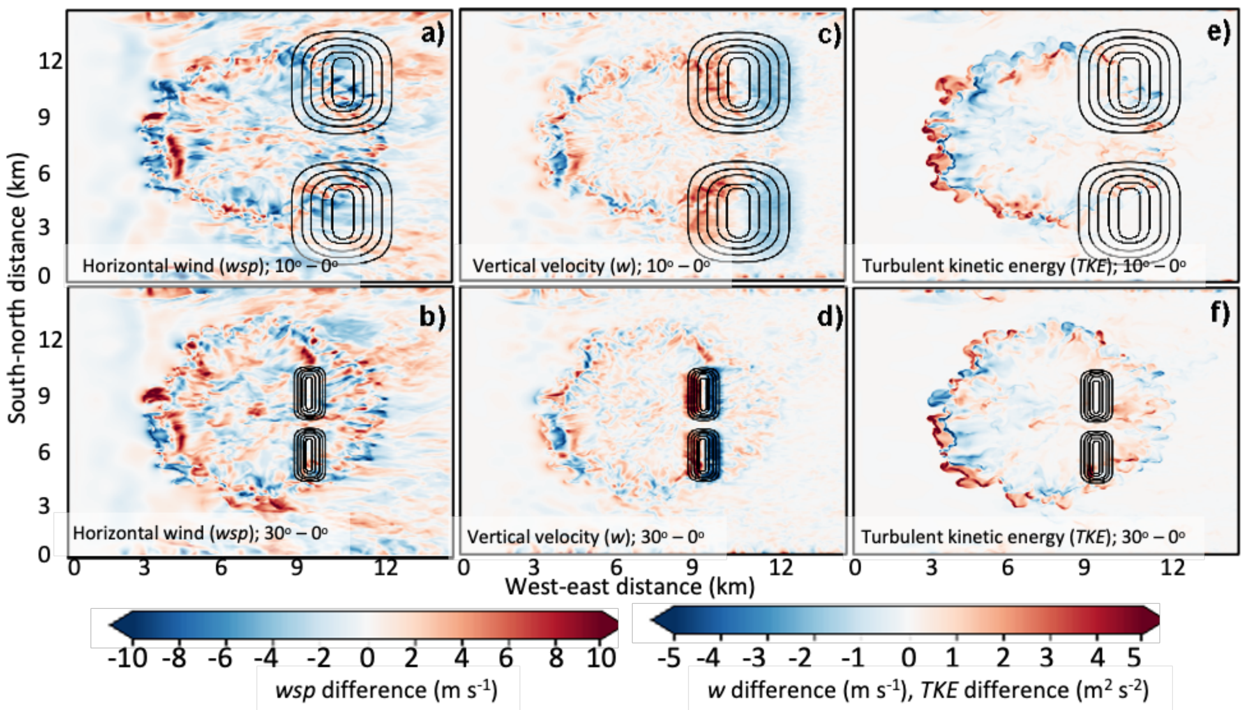

Fig. 9. As Fig. 8, but at 06hh:06min:30s.

c. Long Canyon Simulations

1) SHORT-DISTANCE MICROBURST

Here, we investigate an outflow boundary that passes through horizontally longer canyons (~3 to 6 km) from a microburst that developed at 1.3 km upwind of the canyons (SDM10°LC and SDM30°LC). The outflow boundary in SDM30°LC propagates faster through the canyon and over the ridges compared to SDM10°LC and shows slightly stronger increases in *wsp* (5 to 7 m s^{-1}), w_{up} (4 to 6 m s^{-1}), and *TKE* (4 to 6 m^2 s^{-2}) compared to SDM10°SC (5 to 6 m s^{-1}; 3 to 5 m s^{-1}; 3 to 5 m^2 s^{-2}). Three minutes after the downburst initiation (06h:03min:00s), the leading edge of the outflow boundary has reached the lowest levels of the west-facing slopes and entrance region of SDM10°LC (Fig. 10a, c, e). In contrast, the outflow boundary in SDM30°LC has crested both northern and southern mountains and nearly reached the middle of the canyon

(Fig. 10b, d, f). Strong increases in *wsp* (by ~6 m s^{-1}) are observed at the entrance region and lower walls of the south-facing slope in SDM10°LC (Fig. 10a). In contrast, increases in *wsp* (~4 m s^{-1}) are weaker in the entrance region and within the SDM30°LC compared to SDM10°LC (Fig. 10b). Increased w_{up} is observed along the west-facing slopes with the magnitude increase considerably higher in SDM30°LC (~6 m s^{-1}) compared to SDM10°LC (~2 to 3 m s^{-1}) (Fig. 10c-d). Note that similar to the short canyon simulations, the strongest w_{up} is confined to the canyon walls with little to no enhancement (< 1 m s^{-1}) within the canyon floors in both SDM30°LC and SDM10°LC. Similarly, increases in *TKE* are considerably stronger along the SDM30°LC walls and crests (~6 m^2 s^{-2}) compared to along the west-facing slopes and entrance region in SDM10°LC (~1 to 2 m^2 s^{-2}). In SDM30°LC, no increase in *TKE* is observed along the canyon floor. However, little increase in *TKE* (~1 to 2 m^2 s^{-2}) is observed at the entrance region of the canyon floor in SDM10°LC (Fig. 10e-f).

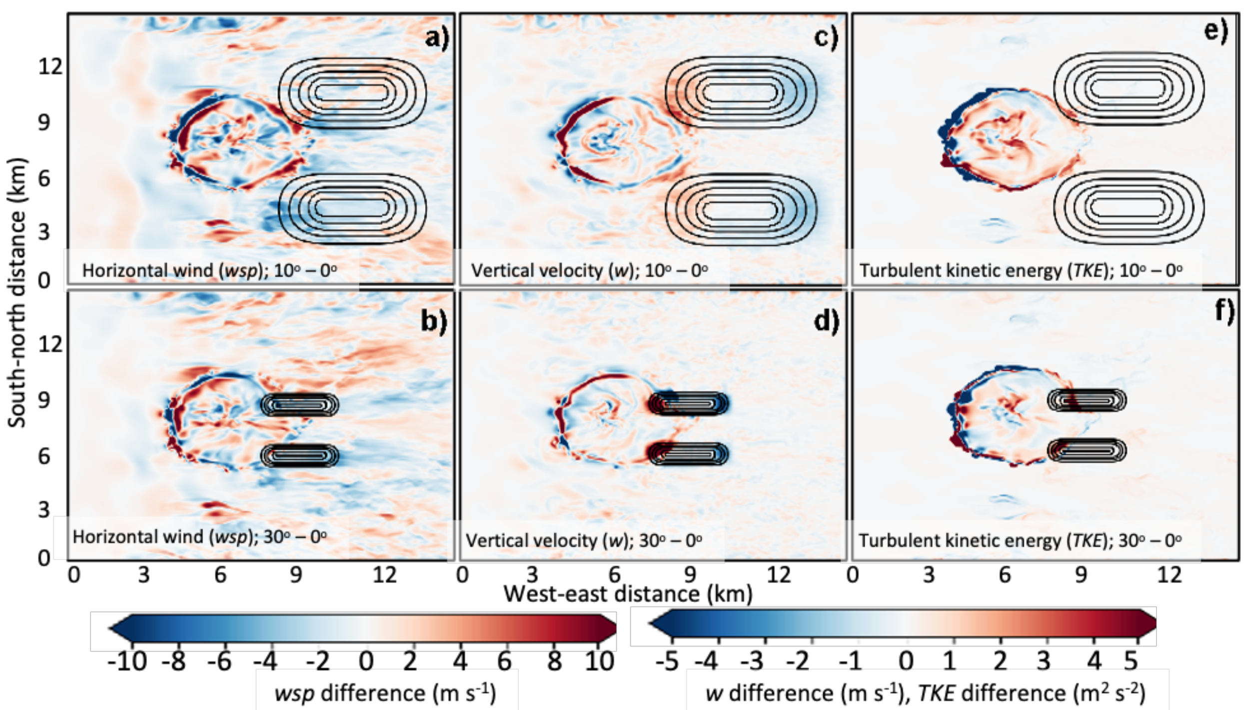

Fig. 10. As Fig. 6 but for differences between a, c, e) SDM10°LC-SDM0°BL and b, d, f) SDM30°LC-SDM0°BL at 06h:03min:00s.

Two minutes later (06h:05min:00s), the outflow boundary in SDM10°LC reaches the crest of both mountains and the middle of the canyon (Fig. 11a, c, e). In contrast, the outflow boundary in SDM30°LC reaches the exit region (Fig. 11b, d, e). In SDM10°LC, *wsp* increase by up to ~5 to 6 m s^{-1} in the middle of the canyon floor, along the crest of the northern mountain, and near the upper west-facing slopes of the southern mountain (Fig. 11a). Similarly, in SDM30°LC, strong increases in *wsp* (~5 to 7 m s^{-1}) are observed in the exit region. However, no increases in *wsp* occur along the crests and canyon walls (Fig. 11b). In SDM10°LC, strong increases in w_{up} of ~5 m s^{-1} is observed along the west-facing slopes and upper walls of the south-facing canyon walls (Fig. 11c). In the SDM30°LC, however, minimal increase in w_{up} (< 1 m s^{-1} at the canyon floor's exit region) is observed along the leading edge of the outflow boundary (Fig. 11). Note that similar to the short-canyon simulations, residual post-boundary strong *w* is still possible along the western and eastern slopes as shown in SDM30°LC. In SDM10°LC, an increase in *TKE* (~5 m^2 s^{-2}) is observed along both the north- and south-facing canyon walls, as well as along the middle of the canyon (~3 m^2 s^{-2}) (Fig. 11e). In SDM30°LC, little increase in *TKE* (~1 - 2 m^2 s^{-2}) is observed in the exit region (Fig. 11f). Additionally, along the crest and eastern slopes of the SDM30°LC southern and northern mountains, *TKE* also increases by up to ~5 to 6 m^2 s^{-2} behind the exiting outflow boundary.

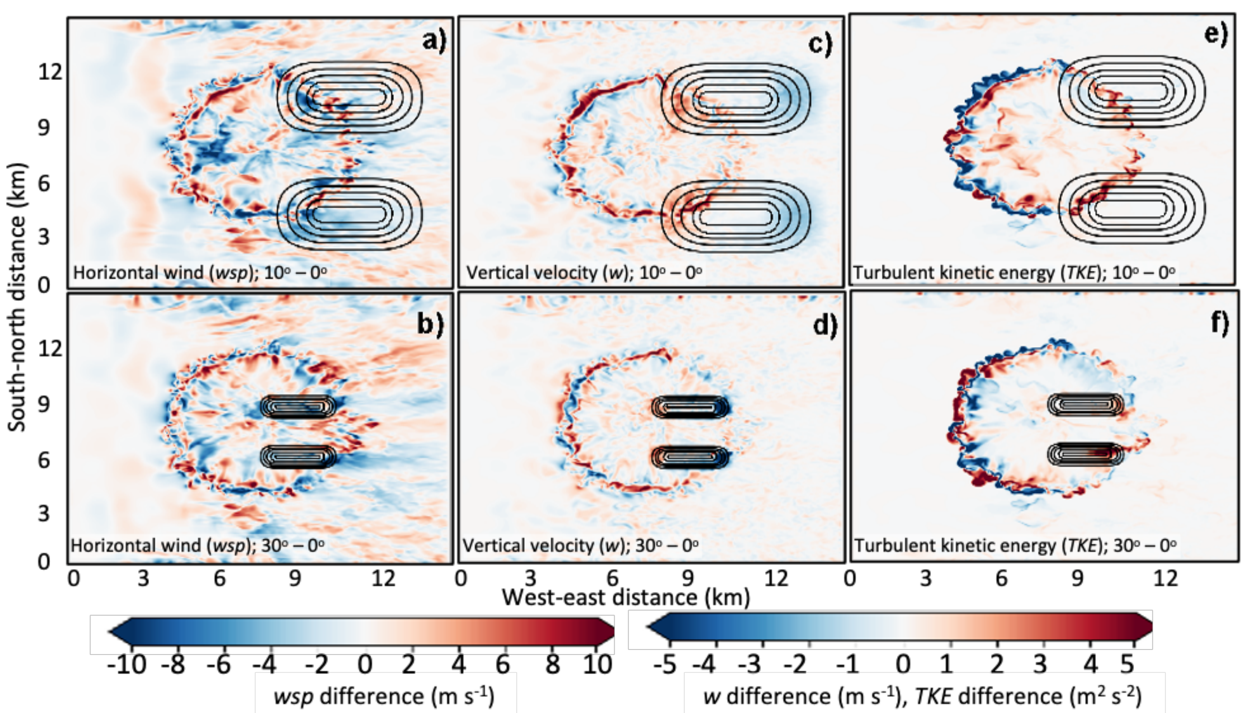

Fig. 11. As Fig. 10, but at 06h:05min:00s.

2) LONG-DISTANCE MICROBURST

Here, we investigate long-canyon influence on a microburst outflow boundary that is generated 3.3 km from the canyon entrance (LDM10°LC and LDM30°LC). Although the outflow boundary in LDM30°LC propagates faster through the canyon and over the mountains compared to LDM10°SC, the increase in *wsp* is weaker in LDM30°LC compared to LDM10°LC (Fig. 10a-b). Four minutes and 30 seconds after microburst initialization, in LDM10°LC the outflow boundary reaches the entrance region (Fig. 12a, c, e). Conversely, the outflow boundary in LDM30°LC reaches the west-facing slopes and crests of both southern and northern mountains and nears the middle of the canyon floor (Fig. 12b, d, f). Weak increases in *wsp* are observed along the canyon floor in both LDM10°LC (~3 to 4 m s^{-1}) and LDM30°LC (~2 to 3 m s^{-1}), with little to no (< 0.5 m s^{-1}) increase in *wsp* elsewhere in either simulation (Fig. 12a-b). w_{up} is stronger along the west-facing slopes and canyon walls in LDM30°LC (~5 m s^{-1}) compared to the western slopes and entrance region in LDM10°LC (~1 to 3 m s^{-1}) (Fig. 12c-d). Similarly, in LDM30°LC, weak increases in *TKE* occur on the crest of the northern mountain (~2 to 3 m^2 s^{-2}) with no increase in *TKE* along the outflow boundary elsewhere along the walls and canyon (Fig. 12f). Conversely, in LDM10°LC, *TKE* negligibly increases (~0.5 to 1 m^2 s^{-2}) within the entrance region of the canyon (Fig. 12e).

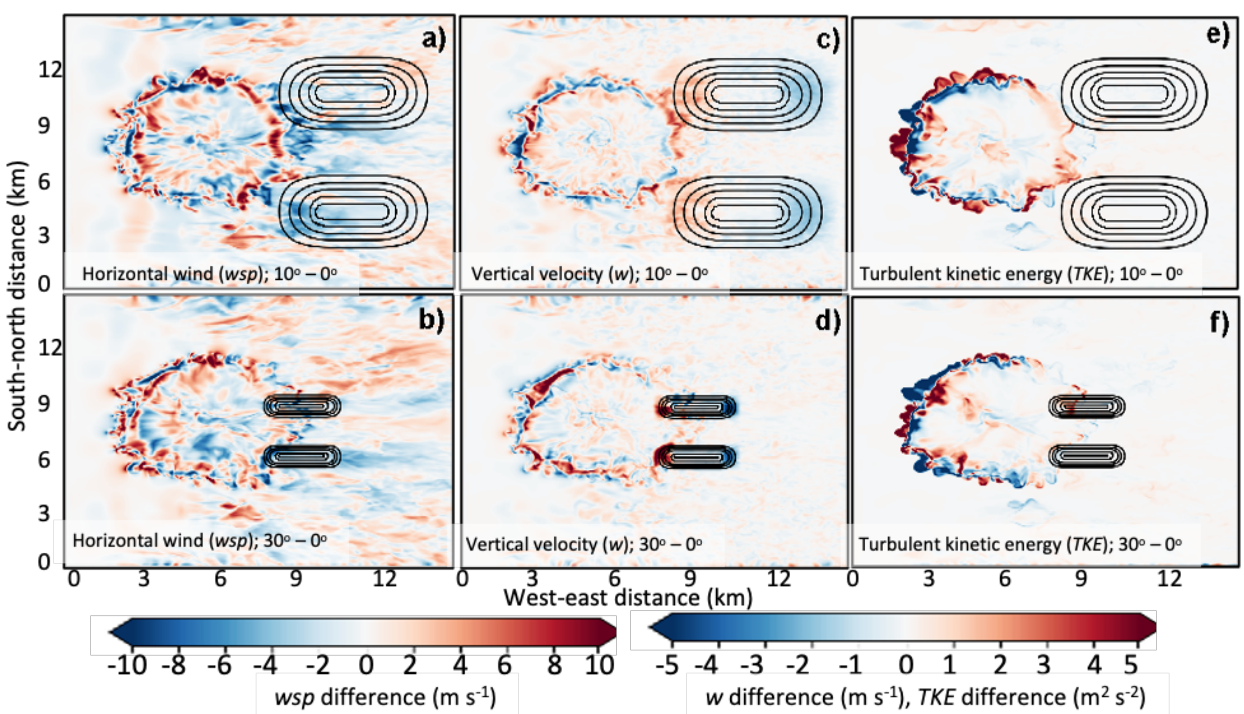

Fig. 12. As Fig. 10, but for a, c, e) LDM10°LC-LDM0°BL and b, d, f) LDM30°LC-DM0°BL at 06h:04min:03s.

A few minutes later (06h:06min:30s), the outflow boundary in LDM10°LC has reached the upper part of the south- and north-facing canyon walls and has neared the middle of the canyon (Fig. 13a, c, e). Conversely, in LDM30°LC the outflow boundary has mostly cleared past the mountains and canyon at this time (Fig. 13b, d, e). Other than some weak residual increase in *wsp* (~3 to 4 m s^{-1}) within the exit region in LDM30°LC, and some post-boundary upward and downward *w* along the western and eastern slopes, the terrain in LDM30°LC no longer affects the leading edge of the outflow boundary (Fig. 13b, d, e). In contrast, in LDM10°LC, *wsp* increase (by ~4 to 5 m s^{-1}) along the canyon floor, and along portions of the canyon walls (Fig. 13a). Similarly, in LDM10°LC, w_{up} increases by up to ~3 to 4 m s^{-1} along the upper part of the west-facing slopes, but less so along the canyon floor (< 0.5 m s^{-1}) (Fig. 13c). Lastly, in LDM10°LC *TKE* negligibly increases by ~0.5 to 1 m^2 s^{-2} within and along the canyon floor and walls (Fig. 13e).

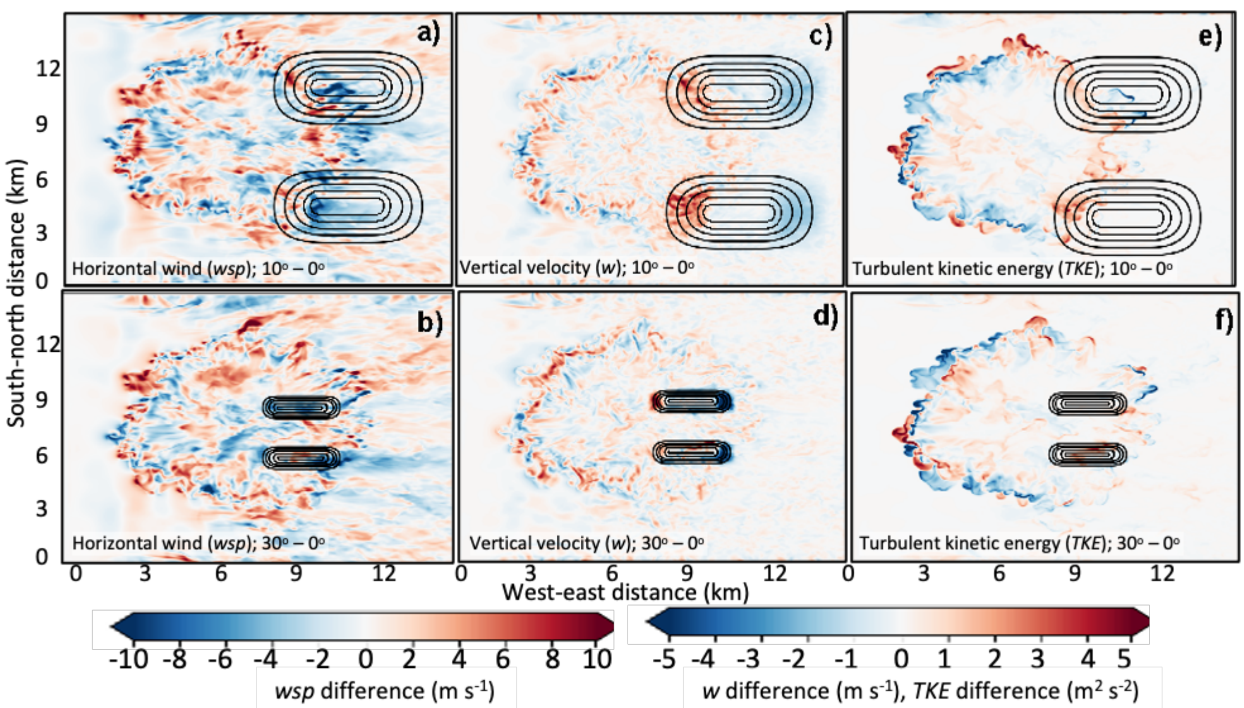

Fig. 13. As Fig. 12, but 06h:06min:30s.

d. Quantifying Wind and Turbulence Changes for All Microburst and Slope Scenarios

In both short- and long-distance canyon simulations, *wsp*, w_{up}, and *TKE* within the canyons and along the canyon walls are stronger when the microburst is closer to the canyons compared to when the microburst is farther from the canyons. To further illustrate these results, the maximum increase of each atmospheric variable during the microburst interaction with the canyons is calculated along west-east cross-sections at 0, 50, 150, and 250 m AGL (Tables 3-4; Fig. 3a). SDMs are more impactful on short and long canyons compared to LDM. Tin he maximum increase in *wsp* at 10 m AGL is stronger in the SDM simulations (3.1 to 6.6 m s^{-1} in SDM10°SC and SDM30°SC; 3.4 to 6.9 m s^{-1} in SDM10°LC, SDM30°LC) compared to the LDM simulations (3.3 to 4.7 m s^{-1} in LDM10°SC and LDM30°SC; 2.4 to 5.7 m s^{-1} in LDM10°LC and LDM30°LC) (Tables 2-3). Similarly, the maximum increase in w_{up} is stronger in the SDM (1.9 to 8.4 m s^{-1} in SDM10°SC and SDM30°SC; 3.8 to 6.4 m s^{-1} in SDM10°LC, SDM30°LC) compared to the LDM simulations (1.7 to 5.3 m s^{-1} in LDM10°SC and LDM30°SC; 2.0 to 5.2 m s^{-1} in LDM10°LC and LDM30°LC). Lastly, the maximum increase in *TKE* is stronger in the SDM simulations (1.2 to 6.6 m^2 s^{-2} in SDM10°SC and SDM30°SC; 1.4 to 6.8 m^2 s^{-2} in SDM10°LC, SDM30°LC) compared to the LDM simulations (0.5 to 4.3 m^2 s^{-2} in LDM10°SC and LDM30°SC; 0.5 to 2.1 m^2 s^{-2} in LDM10°LC and LDM30°LC) (Tables 3-4). In summary, a 2-km difference between the location of the microbursts in SDM and LDM simulations resulted in a reduction in the increase in *wsp* of 0.3 to 3.3 m s^{-1}, w_{up} of 0.1 to 3.1 m s^{-1}, and *TKE* of 0.4 to 5.1 m^2 s^{-2}.

	Short-distance microburst (SDM)			**Long-distance microburst (LDM)**		
	wsp (m s^{-1})	w_{up} (m s^{-1})	*TKE* (m^2 s^{-2})	*wsp* (m s^{-1})	w_{up} (m s^{-1})	*TKE* (m^2 s^{-2})
10° CANYON SLOPE (10°SC)						
	SDM10°SC - SDM0°BL			LDM10°SC - LDM0°BL		
0 m	5.2	2.1	1.4	3.7	1.8	0.9
50 m	5.6	2.8	1.2	3.5	2.7	0.7
150 m	4.1	4.0	3.7	3.3	2.8	0.8
250 m	3.1	3.7	5.1	4.7	3.1	0.5

30° CANYON SLOPE (30°SC)						
	SDM30°SC - SDM0°BL			LDM30°SC - LDM0°BL		
0 m	6.6	1.9	1.4	4.0	1.7	0.9
50 m	5.7	3.4	1.4	4.0	3.1	0.7
150 m	4.5	5.1	5.6	3.0	4.9	0.8
250 m	6.5	8.4	6.6	4.2	5.3	4.3

Table 3. Maximum differences between baseline (0°BL) and short-distance canyon (SC) simulations (10° and 30° slopes) for short and long-distance microbursts: horizontal wind speed (*wsp*) (m s^{-1}) at z = 10 m, upward vertical velocity (w_{up}) (m s^{-1}) at z = 50 m, and turbulence kinetic energy (*TKE*) (m^2 s^{-2}) at z = 10 m. Values are calculated along west-east horizontal cross-sections following the contoured isolines at 0, 50, 150, and 250 m AGL shown in Fig. 3a.

	Short-distance microburst (SDM)			**Long-distance microburst (LDM)**		
	wsp (m s^{-1})	w_{up} (m s^{-1})	*TKE* (m^2 s^{-2})	*wsp* (m s^{-1})	w_{up} (m s^{-1})	*TKE* (m^2 s^{-2})
10° CANYON SLOPE (10°LC)						
	SDM10°LC - SDM0°BL			LDM10°LC - LDM0°BL		
0 m	6.4	4.2	3.5	5.3	2.1	0.9
50 m	5.5	3.8	2.6	5.2	3.5	1.0
150 m	5.6	3.9	4.6	4.9	2.9	1.1
250 m	5.3	4.9	5.6	5.7	2.0	0.5
30° CANYON SLOPE (30°LC)						
	SDM30°LC - SDM0°BL			LDM30°LC - LDM0°BL		
0 m	6.6	5.0	1.4	4.1	2.2	0.8
50 m	6.7	6.0	3.7	3.4	5.0	1.0
150 m	6.9	6.4	5.1	4.4	5.2	1.2
250 m	3.4	6.4	6.8	2.4	5.1	2.1

Table 4. As Table 3, but for the long-distance canyon (LC) simulations.

For LDM simulations (LDM10°SC, LDM30°SC; DM10°LC, LDM30°LC; Table 3-4) the steepness of the canyon walls has less influence on *wsp* and *TKE* associated with the outflow boundary, compared to the SDM simulations (SDM10°SC, SDM30°SC; SDM10°LC, SDM30°LC) where *wsp*, w_{up}, and *TKE* increase more within the 30°-sloped compared to the 10°-sloped canyons. In the SDM simulations, the maximum increase in *wsp*, w_{up}, and *TKE* is stronger within the 30°-sloped (3.4 to 6.9 m s^{-1}; 1.9 to 8.4 m s^{-1}; 1.4 to 6.8 m^{2} s^{-2} in SDM30°SC and SDM30°LC) compared to the 10°-sloped canyons (3.1 to 5.6 m s^{-1}; 2.1 to 4.9 m s^{-1}; 1.4 to 5.6 m^{2} s^{-2} in SDM10°SC and SDM10°LC) (Tables 3-4). These results agree with other microburst studies that observed increasing topographic enhancement of microburst flow over hills and escarpments with increasing slope steepness (Letchford and Illidge 1999; Wood et al. 2001; Mason et al. 2007, 2010). In summary, a difference in slope of 20° created a reduction in the increase in *wsp* of 0.2 to 3.4 m s^{-1}, w_{up} of 0.8 to 4.6 m s^{-1}, and *TKE* of 0.1 to 1.5 m^{2} s^{-2}.

In the LDM simulations, however, differences in canyon slope steepness are not a strong determining factor on the increase in *wsp* along the leading edge of outflow boundaries. Specifically, the maximum increase in *wsp* is weaker within the 30°-sloped (2.4 to 4.1 m s^{-1} in LDM30°SC and LDM30°LC) compared to the 10°-sloped canyons (3.3 to 5.7 m s^{-1} in LDM10°SC and LDM10°LC) (Tables 3-4). Conversely, the maximum increase in w_{up} and *TKE* are slightly stronger within the 30°-sloped (1.7 to 5.3 m s^{-1}; 0.7 to 4.3 m^{2} s^{-2} in LDM30°SC and LDM30°LC) compared to the 10°-sloped canyons (1.8 to 3.5 m s^{-1}; 0.5 to 1.1 m^{2} s^{-2} in LDM10°SC and LDM10°LC). Note, however, there is a strong outlier along the 250 m isoline in the LDM30°SC of 4.3 m^{2} s^{-2}, without which, the differences in *TKE* between the 10°- and 30°-sloped canyons range between 0.5-0.9 m^{2} s^{-2}. Regardless, differences in canyon slope steepness have no influence on the increase in *wsp*, but steeper slopes may lead to slightly stronger increases in w_{up} and *TKE* along outflow boundaries from microbursts that initiate farther from the canyons.

Across all eight canyon simulations, the location of the maximum increase in atmospheric parameters varies spatially depending on slope orientation and elevation. For example, the increase in *wsp* is generally strongest (> 3 to 5 m s^{-1}) at the lower levels of the canyon (0 – 50 m) (Tables 3-4) and is typically maximized towards the exit region of the canyon floors in both SC and LC simulations. This may be related to the narrow topography channeling the winds through the center and out the end of the canyons near the surface which is often observed in other studies of canyon effects on local winds (Goens and Andrews 1998; Brown 2002; Esperanza Investigation Team 2006; Coen and Riggan 2010; Sharples et al. 2010).

Alternatively, the increase in w_{up} is strongest along the upper part of the canyon walls and crests (Tables 3-4), and the peak w_{up} was typically observed along the west-facing slopes. Similarly, the maximum increase in *TKE* was predominately stronger along the upper canyon walls and crests in both short- and long-distance microburst simulations (note the only exception is in LDM10°SC) (Tables 3-4). These observations agree with other studies of turbulence and upward motion within narrow valleys where strong gradients in the mean flow results in significant shear production of *TKE* up the slope and at the crest of ridgelines (Mason et al. 2007 2010; Schmidli 2013).

e. Comparisons of Topographic Multipliers For Short- and Long-Distance Canyons

For both LDM and SDM simulations, the maximum M_t is also higher when the microburst is close to the canyons compared to when the microburst initiates farther from the canyons. Specifically, maximum M_t is generally higher in SDM (*wsp* increases of 18 to 53 % in SDM10°SC and SDM30°SC; 10 to 57 % in SDM10°LC and SDM30°LC) compared to the LDM simulations (12 to 30% in LDM10°SC and LDM30°SC; 6 to 31% in LDM10°LC and LDM30°LC) (Table 5).

	Short Canyon		**Long Canyon**	
	SDM	**LDM**	**SDM**	**LDM**
10° CANYON SLOPE				
0 m	1.3	1.1	1.5	1.2
50 m	1.4	1.2	1.4	1.3
150 m	1.3	1.2	1.4	1.3
250 m	1.2	1.3	1.4	1.3
30° CANYON SLOPE				
0 m	1.4	1.2	1.5	1.3
50 m	1.4	1.2	1.5	1.2
150 m	1.4	1.1	1.6	1.3
250 m	1.5	1.3	1.1	1.1

Table 5. Maximum topographic multiplier (at z = 10 m) for simulation of short- and long-distance canyons calculated along west-east horizontal cross-sections following 0, 50, 150, and 250 m AGL contours for short- and long-distance microbursts.

In the SDM simulations (SDM10°SC, SDM30°SC; SDM10°LC, SDM30°LC), the steeper slopes along the canyon walls have a stronger influence on maximum M_t compared to the LDM simulations (LDM10°SC, LDM30°SC; LDM10°LC, LDM30°LC) where steeper slopes do not result in higher maximum M_t. For the SDM simulations, maximum M_t is higher within the 30° compared to the 10° canyons for both short (36 to 53 % SDM30°SC; 18 to 32% in SDM10°SC) and long distance (10 to 57% in SDM30°LC; 36 to 48% in SDM10°LC) canyons. The only exception is along the 250 m cross-section of the long canyons where maximum M_t is higher in the SDM10°LC (42 % increase in wind speed) compared to the SDM30°LC (10 % increase in wind speed). In the LDM simulations, however, the range of maximum M_t is comparable between 10° (14 to 30 % in LDM10°SC; 23 to 31% in LDM10°LC) and 30° (12 to 26 % in LDM30°SC; 6 to 25% in LDM30°LC) canyons (Table 5). These results re-iterate that when the microburst develops farther from the canyons, slope steepness is not a strong factor in determining the enhancement of horizontal outflow winds.

The maximum M_t across each west-east cross-section is almost always higher in the LC, compared to the SC simulations (Table 5). These differences in maximum M_t may be related to differences in the orientation and length between the short- and long-distance canyons, which may determine their overall terrain-channeling potential. Since the maximum *wsp* is typically observed towards the canyon exit region in all simulations, terrain-channeling must be present and most effective as the outflow boundary reaches the exit region. In the SC simulations, the average propagation speed of the leading edge of the outflow boundaries at the time they reach the canyon floor's exit region ranges between 17.7 and 23.3 m s^{-1}. Conversely, in the LC simulations, the average propagation speed along the outflow boundaries at the canyon floor's exit region is slower between 14.2 and 17.5 m s^{-1}, likely due to an increase in drag along the horizontally longer mountains. Therefore, LC tend to slow down the advancing outflow boundaries, allowing for longer durations of canyon-channeling of *wsp* compared to the SC, where the boundaries propagate through the canyons quickly leaving little time for terrain-channeling.

4. Conclusions

This study quantifies the enhancement of microburst outflow boundary winds and turbulence within canyons using the WRF-LES simulation capability. Simulated microburst outflow boundaries propagate through short- (~1.5 to 4.5 km) and long-distance canyons (~3 to 6 km) where canyon walls have slopes of 10° and 30°. These canyon simulations are compared to microburst outflow boundary characteristics in flat terrain. Microbursts were placed close to the canyon, so that the maximum in outflow boundary wind speed occurs at the canyon entrance, and farther away to study the influence of topography on outflow boundaries with weaker wind speeds. The main findings from this analysis are:

- Compared to flat terrain, an increase in *wsp*, w_{up}, and TKE are observed within the canyon (Table 3-5)
- SDM produce stronger canyon-induced enhancements in *wsp* (3 m s^{-1}), w_{up} (3 m s^{-1}), *TKE* (4.7 m^2 s^{-2}), and M_t (28 %) in the canyons and along the canyon walls compared to LDM.
- For canyons located closer to the microburst, the increase in *wsp* (3.2 m s^{-1}), w_{up} (0.8-4.6 m s^{-1}), *TKE* (1.4 m^2 s^{-2}) and M_t (29%) is generally stronger in the canyon and along the walls of the 30°-sloped compared to the 10°-sloped canyons. When the canyons are farther from the microburst, steeper slopes do not enhance wind and turbulence in the canyon in either short- or long-distance canyons.
- For both SD and LD canyons, the maximum increase in *wsp* is mostly observed near the canyon floors and towards the exit region of the canyons regardless of the proximity to the microburst. Conversely, the maximum increase in w_{up} and *TKE* is mostly observed at higher elevations on the walls and along the canyon crests in both SDC and LDC.

Results from this study provide an initial quantification of canyon-enhancement of microburst outflow winds and turbulence using idealized numerical simulations. A future study could expand upon these experiments and investigate the influence of other important parameters such as the magnitude and horizontal extent of the cold bubble perturbation, altering the background atmospheric stability and shear profile, changing the surface roughness length, or altering the height of the mountains. Additional analysis of these parameters could benefit fire weather forecasters and emergency responders who assess the potential dangers of outflow boundaries in and around ongoing canyon wildfires.

Acknowledgement.

This research is supported through an award L17AC00227 ("JFSP Project 17-1-05-2 Evaluating thunderstorm outflow boundaries in WRF-Fire") from the Bureau of Land Management (BLM) as part of the Joint Fire Science Program under the subject opportunity FA-FON0017-0002. This work utilized the RMACC Summit supercomputer, which is supported by the National Science Foundation (awards ACI-1532235 and ACI-1532236), the University of Colorado Boulder, and Colorado State University. The Summit supercomputer is a joint effort of the University of Colorado Boulder and Colorado State University. We would like to thank Prof. Julie Lundquist for the helpful comments.

Data Availability Statement.

The WRF model code (https://doi.org/10.5065/D6MK6B4K, Skamarock et al., 2008) is publicly available at http://www2.mmm.ucar.edu/wrf/users/ (last access: 11 June 2020). Model output data for hours 6-7 h and analysis code including namelist.input, input soundings, and auxiliary terrain netcdf files needed to run the simulations and create the figures are located at https://github.com/nluchett/wrf_canyon_experiment.

REFERENCES

Benjamin, T. B., 1968: Gravity currents and related phenomena. *Journal of Fluid Mechanics*, **31**, 209-248, https://doi.org/10.1017/S0022112068000133.

Brown, H., 2002: Thirtymile Fire: fire behavior and management response. *Fire Management Today*, **62(3)**, 23–30. [Available at https://www.fs.usda.gov/sites/default/files/fire-management-today/62-3.pdf]

Charba, J., 1974. Application of gravity current model to analysis of squall-line gust front. *Mon. Wea. Rev.*, **102**, 140-156, https://doi.org/10.1175/1520-0493(1974)102<0140:AOGCMT>2.0.CO;2.

Coen, J.L., and P. J. Riggan, 2010: A landscape-scale wildland fire study using a coupled weather-wildland fire model and airborne remote sensing. *Proceedings of 3rd fire behavior and fuels* conference, Birmingham, AL, International Association of Wildland Fire, 11 pp.

Draeger, R., 2016: Frog Fire Fatality. USDA Forest Service Learning Review Report. [Available at https://www.wildfirelessons.net/HigherLogic/System/DownloadDocumentFile.ashx?DocumentF ileKey=c197dde6-ced5-01a2-0b0d-2b735e4934ea&forceDialog=0]

Dupuy, J. L., J. Maréchal, D. Portier, and J. C. Valette, 2011: The effects of slope and fuel bed width on laboratory fire behavior. *International Journal of Wildland Fire*, **20(2)**, 272-288. https://doi.org/10.1071/WF09075.

Esperanza Investigation Team, 2006: Esperanza Fire accident investigation factual report, Riverside County, California. [Available at http://www.fire.ca.gov/fire_protection/downloads/esperanza_00_complete_final_ draft_05_01_2007.pdf]

Friedrich, K., D.E. Kingsmill, and C.R. Young, 2005: Misocyclone characteristics along Florida gust fronts during CaPE. *Mon. Wea. Rev.*, **133**, 3345– 3367, https://doi.org/10.1175/MWR3040.1.

Fujita, T. T., and R. M. Wakimoto, 1983: Microbursts in JAWS depicted by Doppler radars, PAM, and aerial photographs. *Preprints, 21st Conference on Radar Meteorology,* Edmonton, Canada, American Meteorological Society, Boston, 638-645.

Fujita, T. T., 1985: The Downburst - Microburst and Macroburst. Report of Projects NIMROD and JAWS. SMRP, University of Chicago, Chicago, 122 pp.

Goens, D. W., and P. L. Andrews, 1998: Weather and fire behavior factors related to the 1990 Dude Fire near Payson, AZ. NWCG Wildland Fire Leadership Development Program. [Available at https://www.nwcg.gov/sites/default/files/wfldp/docs/sr-dude-related-factors.pdf]

Grant, L. D., and S. C. van den Heever, 2016: Cold pool dissipation. *J. Geophys. Res. Atmos.*, **121**, 1138–1155, doi:10.1002/2015JD023813.

Haines, D. A., 1988: Downbursts and wildland fires: a dangerous combination. *Fire Management Today*, **49**, 8–10. [Available at https://www.frames.gov/documents/usfs/fmt/fmt_64-1.pdf]

Hardy, K., and L. K. Comfort, 2015: Dynamic decision processes in complex, high-risk operations: The Yarnell Hill Fire, June 30, 2013. *Saf. Sci.*, **71**, 39–47, https://doi.org/10.1016/j.ssci.2014.04.019.

Hawley, L. F., 1926: Theoretical considerations regarding factors which influence forest fires. *Journal of Forestry*, **24(7)**, 756-763. https://doi.org/10.1093/jof/24.7.756.

Johnson, R. H., R. S. Schumacher, J. H. Ruppert, D. T. Lindsey, J. E. Ruthford, and L. Kriederman, 2014: The role of convective outflow in the Waldo canyon fire. *Mon. Wea. Rev.*, **142**, 3061–3080, https://doi.org/10.1175/MWR-D-13-00361.1.

Jorgensen, D.P., Z. Pu, P.O. Persson, and W. Tao, 2003: Variations associated with cores and gaps of a pacific narrow cold frontal rainband. *Mon. Wea. Rev.*, **131**, 2705–2729, https://doi.org/10.1175/1520-0493(2003)131<2705:VAWCAG>2.0.CO;2.

Karels, J., and M. Dudley, 2013: Yarnell Hill Fire Serious Accident Investigation Report. Arizona State Forestry Division Rep., 116 pp., https://docs.google.com/file/d/0B36DIycSgbzWSUtjNkl1Z2ROT0k/edit.

Letchford, C., and Illidge, 1999: Turbulence and topographic effects in simulated thunderstorm downdrafts by wind tunnel jet. *Proc,. 10th ICWE*, Copenhagen, 1999.

Liu, N., H. Chen, X. Xie, L. Zhang, B. Yao, J. Zhu, and Y. Shan, 2014: Effect of slope on spread of a linear flame front over a pine needle fuel bed: experiments and modelling. *International Journal of Wildland Fire*, **23(8)**, 1087-1096. https://doi.org/10.1071/WF12189

Marion, G. R., and R. J. Trapp, 2018: The dynamical coupling of convective updrafts, downdrafts, and cold pools in simulated supercell thunderstorms. *Journal of Geophysical Research: Atmospheres,* **124**, 664-683.

Mason, M. S., G. S. Wood, and D. F. Fletcher, 2007: Impinging jet simulation of stationary downburst flow over topography. *Wind and Structures*, **10(5)**, 437-462. https://doi.org/10.12989/was.2007.10.5.437

Mason, M. S., G. S. Wood, and D. F. Fletcher, 2010: Numerical investigation of the influence of topography on simulated downburst wind fields. *J. Wind Eng. Ind. Aerodyn.*, **98**, 21–33, https://doi.org/10.1016/j.jweia.2009.08.011.

Mirocha, J. D., J. K. Lundquist, and B. Kosović, 2010: Implementation of a nonlinear subfilter turbulence stress model for Large-Eddy Simulation in the advanced research WRF model. *Mon. Wea. Rev.*, **138**, 4212–4228, https://doi.org/10.1175/2010MWR3286.1.

Mirocha, J., G. Kirkil, E. Bou-Zeid, F. K. Chow, and B. Kosović, 2013: Transition and equilibration of neutral atmospheric boundary layer flow in one-way nested Large-Eddy Simulations using the Weather Research and Forecasting model. *Mon. Wea. Rev.*, **141**, 918–940, https://doi.org/10.1175/MWR-D-11-00263.1.

Moeng, C., J. Dudhia, J. Klemp, and P. Sullivan, 2007: Examining two-way grid nesting for Large Eddy Simulation of the PBL Using the WRF Model. *Mon. Wea. Rev.*, **135**, 2295–2311, https://doi.org/10.1175/MWR3406.1.

Monastersky, R., 1987: Mastering the microburst. *Science News*, 185-187.

Nunalee, C. G., B. Kosović, and P. E. Bieringer, 2014: Eulerian dispersion modeling with WRF-LES of plume impingement in neutrally and stably stratified turbulent boundary layers. *Atmospheric Environment*, **99**, 571-581. https://doi.org/10.1016/j.atmosenv.2014.09.070.

Paez, G., M. Strojnik, and M. K. Scholl, 2015: Analysis of propagation of complex fire: Case of the Yarnell Hill Fire 1. *Proc. SPIE*, **9608**, 96081L, https://doi.org/10.1117/12.2191725.

Potter, B. E., and J. R. Hernandez, J. R., 2017: Downdraft outflows: climatological potential to influence fire behavior. *International Journal of Wildland Fire*, **26(8)**, 685-692. https://doi.org/10.1071/WF17035.

Rothermel, R. C., 1993: Mann Gulch fire: A race that couldn't be won. Gen. Tech. Rep. INT-299. Ogden, UT: US Department of Agriculture, Forest Service, Intermountain Research Station. 10 pp., 299.

Sasaki, Y. K., and T. L. Baxter, 1986: The gust front. *Thunderstorm Morphology and Dynamics*, E. Kessler, Ed., University of Oklahoma Press, 187–196.

Schmidli, J., 2013: Daytime heat transfer processes over mountainous terrain. *J. Atmos. Sci.*, **70**, 4041–4066, https://doi.org/10.1175/JAS-D-13-083.1.

Sharples, J. J., 2008: Review of formal methodologies for wind–slope correction of wildfire rate of spread. *International Journal of Wildland Fire*, **17(2)**, 179-193. https://doi.org/10.1071/WF06156.

Sharples, J., A. M. Gill, J. W. Dold, 2010: The trench effect and eruptive wildfires: lessons from the King's Cross Underground disaster. *Proceedings of Australian Fire and Emergency Service Authorities Council 2010 Conference*, Darwin, Australia. [Available at http://www.maths. manchester.ac.uk/~jwd/articles/10-TEaEW.pdf.]

Sharples, J. J., R. H. D. McRae, C. Simpson, P. Fox-Hughes, and C. Clements, 2017: Terrain-controlled airflows. *Fire Manage. Today*, **75**, 20–24.

Simpson, J.E., and R.E. Britter, 1980: A laboratory model of an atmospheric mesofront. *Quarterly Journal of the Royal Meteorological Society*, **106**, 485-500. doi:10.1002/qj.49710644907.

Sullivan, A. L., 2009: Wildland surface fire spread modelling, 1990–2007. 3: Simulation and mathematical analogue models. *International Journal of Wildland Fire*, **18(4)**, 387-403. https://doi.org/10.1071/WF06144.

Sullivan, A. L., J. J. Sharples, S. Matthews, and M. P. Plucinski, 2014: A downslope fire spread correction factor based on landscape-scale fire behavior. *Environmental Modelling & software,* **62**, 153-163. https://doi.org/10.1016/j.envsoft.2014.08.024.

United States Department of the Interior (USDI), 1976: Accident Report - Battlement Creek fire fatalities and injury, July 17, 1976. United States Department of Interior, Unpublished Report on file at National Interagency Fire Center, Boise, ID, 125 p.

United States Department of the Interior (USDI)/ United States Department of the Agriculture (USDA), 1994: South Canyon Fire Investigation Report, Report of the South Canyon fire accident investigation team. Report 573-183, US Government Printing Office, Region 8, Washington DC. 234 p.

Viegas, D.X. 2005. A mathematical model for forest fire blow-up. *Combustion Science and Technology,* **177**, 1–25. https://doi.org/10.1080/00102200590883624.

Viegas, D.X., and A. Simeoni, 2010: Eruptive behavior of forest fires. *Fire Technology*. **47(24)**, 303. https://doi.org/10.1007/s10694-010-0193-6.

Wakimoto, R. M., C. J. Kessinger, and D. E. Kingsmill, 1994: Kinematic, thermodynamic, and visual structure of low-reflectivity microbursts. *Mon. Wea. Rev.*, **122**, 72–92, https://doi.org/10.1175/1520-0493(1994)122<0072:KTAVSO>2.0.CO;2.

Wilson, J. W., R. D. Roberts, C. Kessinger, and J. McCarthy, 1984: Microburst wind structure and evaluation of Doppler radar for airport wind shear detection. *J. Climate Appl. Meteor.*, **23**, 898–915, https://doi.org/10.1175/1520-0450(1984)023<0898:MWSAEO>2.0.CO;2.

Wood, G. S., K. C. Kwok, N. A. Motteram, and D. F. Fletcher, 2001: Physical and numerical modelling of thunderstorm downbursts. *Journal of Wind Engineering and Industrial Aerodynamics*, **89(6)**, 535-552. https://doi.org/10.1016/S0167-6105(00)00090-8.